nature catalysis

ARTICLES

https://doi.org/10.1038/s41929-021-00640-y

Check for updates

Room-temperature electrochemical acetylene reduction to ethylene with high conversion and selectivity

Run Shi[1,7], Zeping Wang[1,2,7], Yunxuan Zhao[1,7], Geoffrey I. N. Waterhouse[3], Zhenhua Li[4], Bikun Zhang[5], Zhimei Sun[5], Chuan Xia[6], Haotian Wang[6] ✉ and Tierui Zhang[1,2] ✉

The selective hydrogenation of acetylene to ethylene in ethylene-rich gas streams is an important process in the manufacture of polyethylene. Conventional thermal hydrogenation routes require temperatures above 100 °C and excess hydrogen to achieve a satisfactory C_2H_2 conversion efficiency. Here, we report a room-temperature electrochemical acetylene reduction system based on a layered double hydroxide (LDH)-derived copper catalyst that offers an ethylene Faradaic efficiency of up to ~80% and inhibits alkane and hydrogen formation. The system affords an acetylene conversion of over 99.9% at a flow rate of 50 ml min^{-1} in a simulated gas feed, yielding high-purity ethylene with an ethylene/acetylene volume ratio exceeding 10^5 and negligible residual hydrogen (0.08 vol.%). These acetylene conversion metrics are superior to most other state-of-the-art strategies. The findings therefore conclusively demonstrate an electrochemical strategy as a viable alternative to current technologies for acetylene-to-ethylene conversions with potential advantages in energy and atom economies.

The industrial manufacture of ethylene (C_2H_4) relies on the pyrolysis of naphtha or saturated C_2 to C_6 hydrocarbons. However, the product streams from these processes contain 0.5–2.0 vol.% acetylene (C_2H_2), which can poison the Ziegler–Natta catalysts used for the polymerization of ethylene to polyethylene[1]. Accordingly, the acetylene content in polymer-grade ethylene streams must be reduced to a few parts per million, stimulating the development of absorption systems or catalytic processes for the selective removal of acetylene from ethylene-rich gas streams.

Solvent absorption was the initial strategy adopted for the selective removal of C_2H_2 (Fig. 1, Route 1) from ethylene-rich gas mixtures[2,3]. In this approach, C_2H_2 is removed by dissolving it in solvents such as *N*,*N*-dimethylformamide or ethyl acetate. However, such methods require large quantities of fossil fuel-derived organic solvents and result in the loss of C_2H_4, and thus are not sustainable from an environmental perspective. Since the 1950s, the selective catalytic hydrogenation of C_2H_2 to C_2H_4 has emerged as a more effective approach for acetylene removal (Fig. 1, Route 2)[4]. Benchmark palladium-based catalysts achieve >90% C_2H_2 conversion with 85% ethylene selectivity at 200 °C (ref. [5]). The thermodynamics and mechanism of C_2H_2 hydrogenation over palladium-based catalysts have been systematically studied in recent years with the aim of lowering reaction temperatures and improving the selectivity towards C_2H_4 (ref. [6–8]). However, in spite of some advances, reaction temperatures of >100 °C are still required to achieve reasonable rates of C_2H_2 conversion. In addition, a molar excess of hydrogen relative to acetylene is required for both laboratory and industrial C_2H_2 hydrogenation reactors to increase the acetylene conversion ratio. However, this approach inevitably results in decreased ethylene selectivity through over-hydrogenation to ethane (C_2H_6). The formation of the latter represents a loss of valuable ethylene and is therefore economically undesirable[9]. Further, the use of excess H_2 generally requires an additional separation step following acetylene hydrogenation and can lead to dangerously thermal run-away processes[10]. Therefore, innovative strategies must be discovered for room-temperature acetylene-to-ethylene conversions that are both energy and atom economic.

In recent years, the electrochemical reduction of light carbon species (for example, CO and CO_2) to produce liquid fuels and other useful chemicals has attracted enormous research attention owing to the mild conditions under which such electrochemical transformations can be performed, as well as the high selectivities for target products and the ability to directly use protons sourced from water oxidation in product synthesis[11–13]. Research into electrochemical acetylene reduction (EAR) dates back to 1971 (ref. [14]), but has received little attention as EAR catalysts generally show poor performance in terms of C_2H_2 conversion rates and product selectivities relative to conventional hydrogenation processes[15–17]. In addition, organic solvents or solid-state electrolytes are often needed for EAR with H_2 due to the very poor solubility (~0.2 mM at 20 °C, 1 atm) and slow mass transfer of acetylene in aqueous media[18–20]. Most EAR studies to date have been carried out in batch H-type electrochemical systems using an acetylene-saturated electrolyte in the absence of ethylene. The feasibility of employing route 3 (Fig. 1) to achieve the complete electroreduction of acetylene in ethylene-rich gas feeds has not yet been explored, motivating a detailed investigation.

In the study reported herein we developed a gas diffusion electrode-based EAR system to overcome acetylene interfacial mass transfer limitations in an alkali electrolyte[21–23]. In this

[1]Key Laboratory of Photochemical Conversion and Optoelectronic Materials, Technical Institute of Physics and Chemistry, Chinese Academy of Sciences, Beijing, China. [2]Center of Materials Science and Optoelectronics Engineering, University of Chinese Academy of Sciences, Beijing, China. [3]School of Chemical Sciences, The University of Auckland, Auckland, New Zealand. [4]College of Chemistry, Central China Normal University, Wuhan, China. [5]School of Materials Science and Engineering, Beihang University, Beijing, China. [6]Department of Chemical and Biomolecular Engineering, Rice University, Houston, TX, USA. [7]These authors contributed equally: Run Shi, Zeping Wang, Yunxuan Zhao. ✉e-mail: htwang@rice.edu; tierui@mail.ipc.ac.cn

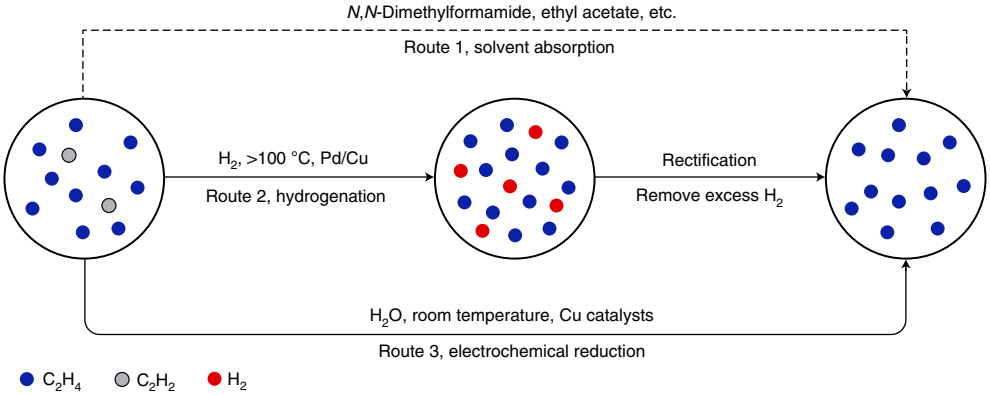

Fig. 1 | Routes for acetylene conversion in ethylene-rich gas streams. Route 1, a traditional solvent absorption process involving complicated pre/post-treatment processes and environmental issues. Route 2, the catalytic semihydrogenation of acetylene at high temperature using H_2, followed by a rectification step to remove excess H_2 in the ethylene stream. Route 3, the electrochemical reduction of acetylene at room temperature using water as the proton source, achieving one-step acetylene-to-ethylene conversion with high efficiency.

approach, gas-phase acetylene diffuses a short distance through a carbon-based gas diffusion layer (GDL) and microporous layer (MPL) to the surface of the catalyst layer via a well-defined gas/electrolyte/catalyst interface, as schematically depicted in Fig. 2a. Room-temperature acetylene electroreduction then occurs at a layered double hydroxide (LDH)-derived copper electrocatalyst, which offers an onset potential of −0.39 V (vs the reversible hydrogen electrode, RHE) for ethylene production. This value is 210 mV greater than the competing hydrogen evolution reaction (HER). Using a simulated ethylene-rich gas mixture (0.5% acetylene) in an EAR flow cell, an acetylene conversion of over 99.9% was achieved with an ethylene selectivity of 90.1%, resulting in the production of high-purity ethylene at a rate of 50 ml min^{-1}. Our results confirm that EAR represents a possible alternative to conventional thermal catalytic hydrogenation processes for the conversion of C_2H_2 into C_2H_4 in ethylene-rich gas streams, offering high activity and selectivity under much milder conditions.

Results

Acetylene electroreduction in the absence of ethylene. In our previous work we have demonstrated the advantages of partially reduced LDHs in regulating the reaction pathways and intermediates in the selective hydrogenation of light carbon species[24,25]. In this work we used an in situ electrochemical reduction strategy to partially reduce CuAl-LDH nanosheets to give an LDH-derived copper catalyst (denoted herein as LD-Cu; Supplementary Figs. 1 and 2). The LD-Cu catalyst was immobilized on the MPL (Fig. 2b,c), with the average thickness of the catalyst layer being 1.0 ± 0.2 μm. To promote the interaction between acetylene and the catalyst, a plane gas chamber with a geometric electrode area of 0.5 cm^2 was first constructed (Supplementary Fig. 3).

The EAR performance of LD-Cu in the absence of ethylene was first investigated. The potentials given here are referenced to the RHE. Linear sweep voltammetry (LSV) measurements performed in 5% C_2H_2 balanced with Ar showed a current density of 2.5 mA cm^{-2} at −0.3 V, which increased to over 70 mA cm^{-2} at −0.6 V (Supplementary Fig. 4). By comparison, experiments conducted using 5% C_2H_4 or pure Ar showed negligible electrochemical response over LD-Cu, indicating that LD-Cu did not catalyse the electroreduction of C_2H_4 in the examined potential range. We also tested the LSV performance of the electrode without an added catalyst. Again, no current density was detected. As shown in Fig. 2d, the onset potential (at 10 mA cm^{-2}) for ethylene production was −0.39 V over LD-Cu, which is 210 mV greater than the competing HER, demonstrating the possibility of a hydrogen-free EAR process (that is, a process that does not require an external H_2 feed for ethylene production). Deuterium-labelled isotope experiments further proved water to be the hydrogen source of the EAR (Supplementary Fig. 5). Figure 2e further reveals that ethylene is the major EAR product over LD-Cu, with the production of C_2H_6 being almost negligible (Faradaic efficiency less than 1%). Some C_4 oligomers (mainly C_4H_6) were also detected, with the Faradaic efficiency towards C_4H_6 decreasing at more negative cathodic potentials (from 11.9% at −0.28 V to 2.7% at −0.60 V). The change in product selectivity with applied potential can be understood in terms of the difference between the reduction potential of the acetylene dimerization reaction ($2C_2H_2 + 2H^+ + 2e^- \rightarrow C_4H_6$, $E° = 1.39$ V) and the acetylene reduction reaction ($C_2H_2 + 2H^+ + 2e^- \rightarrow C_2H_4$, $E° = 0.73$ V). The Faradaic efficiency for ethylene production increased from 39.2 ± 4.2% at −0.28 V to 79.5 ± 5.0% at −0.52 V. At −0.6 V, the Faradaic efficiency decreased slightly to 74.9 ± 0.8%. Judicious selection of the cathodic potential is therefore an important requirement for achieving selective EAR to ethylene. A linear Arrhenius relationship for acetylene conversion was observed at temperatures ranging from 5 to 25 °C (Supplementary Fig. 6), affording an apparent activation energy of 21.4 kJ mol^{-1} at −0.4 V. We also investigated the EAR performance of LD-Cu in an H-cell in which the electrode was immersed in a 5%-C_2H_2-saturated 1 M KOH solution and the GDL was blocked by silicone grease to eliminate any gas diffusion through the GDL. The cell exhibited a non-linear relationship and a dramatically decreased acetylene conversion rate compared with the gas flow system, indicating a solubility-controlled liquid-phase diffusion process as the rate-determining step[26]. As shown in Fig. 2f, the flow electrochemical system with LD-Cu as catalyst provided partial current densities and Faradaic efficiencies for C_2H_4 production around 10-fold and 40% higher, respectively, than previously reported EAR systems (comparative data are provided in Supplementary Table 1)[14,19]. We also investigated the performance of a commercial metallic copper nanoparticle catalyst (denoted here as Cu NPs) in the EAR (Supplementary Figs. 7 and 8). The onset potential gap between ethylene and hydrogen production over Cu NPs was only 140 mV (compared with 210 mV over LD-Cu). For the Cu NPs, the ethylene Faradaic efficiency dramatically decreased at high partial current densities owing to the negative ethylene production onset potential (−0.48 V) and severe competition for the HER. The Tafel slope for ethylene production on Cu NPs was determined to be 180.8 mV dec^{-1}, which is nearly two times higher than that for LD-Cu (96.2 mV dec^{-1}), indicating different EAR reaction kinetics over the two copper-based catalysts (Supplementary Fig. 9).

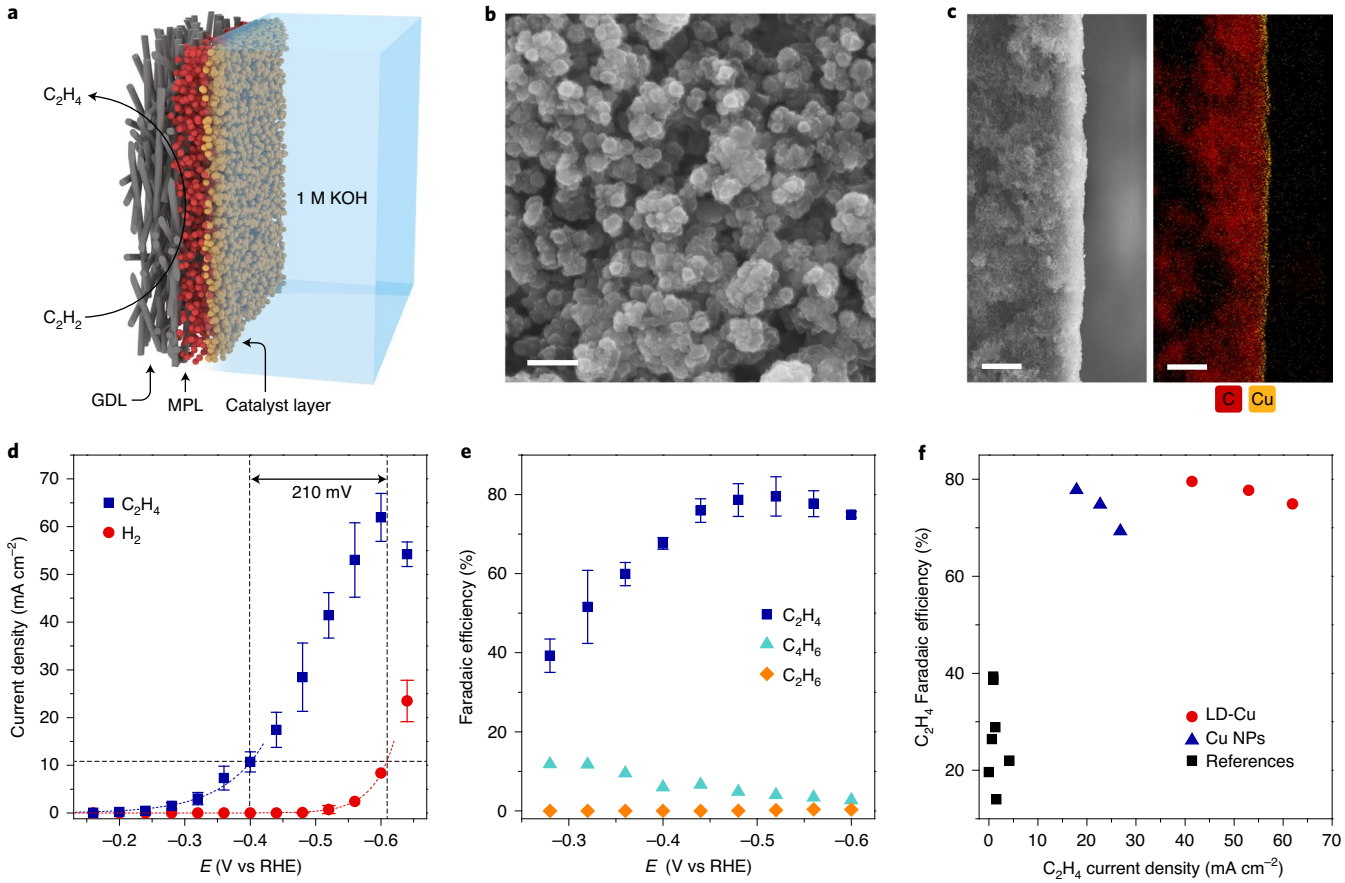

Fig. 2 | Characterization of EAR in a flow system. a, Schematic illustration of the cathode used for the EAR investigation. **b**, SEM image of LD-Cu on the MPL. Scale bar, 200 nm. **c**, Cross-sectional SEM image (left) and corresponding elemental map (right) of LD-Cu on the MPL. Scale bars, 10 μm. **d**, Partial current densities for C_2H_4 and H_2 production over LD-Cu versus applied potentials. Reaction conditions: 5% C_2H_2 with Ar balance as gas source, flow rate 10 ml min^{-1}, 1 M KOH as electrolyte. **e**, Faradaic efficiency profiles of the EAR products versus applied potentials. **f**, Comparison of the C_2H_4 partial current densities and Faradaic efficiencies over LD-Cu, Cu NPs and previously reported catalysts. The error bars represent the standard deviation from at least three independent measurements.

Structural characterization and reaction kinetics analysis. It has been reported that the valence state and coordination environment of copper species can greatly affect thermal hydrogenation reactions of acetylene[27–29]. To gain more insight into the enhanced EAR performance of LD-Cu, the catalyst structure was explored in detail. Figure 3a shows the X-ray photoelectron spectra (XPS) of the CuAl-LDH precursor and a series of LD-Cu catalysts prepared at different electroreduction potentials. For the CuAl-LDH nanosheets, only Cu(II) was detected. Samples reduced in the potential range of −0.3 to −0.6 V were observed to share similar nanoparticle morphologies (Supplementary Fig. 10) with a reduced copper valence state. Cu LMM auger electron spectroscopy (AES) analysis of LD-Cu reduced at −0.5 V revealed a mixture of Cu(0) and Cu(I) species (Supplementary Fig. 11)[30]. The electronic and coordination environments of the Cu species were further investigated by Cu K-edge X-ray absorption near-edge spectroscopy (XANES). The Cu K-edge XANES spectra of LD-Cu in Fig. 3b and Supplementary Fig. 12 show the Cu species to be intermediate between Cu and Cu_2O, implying a positively charged $Cu^{\delta+}$ state ($0<\delta<1$). In contrast, the Cu K-edge XANES spectrum for Cu NPs closely resembles that of the Cu reference foil, indicating that Cu(0) is the dominant oxidation state. Figure 3c shows Fourier transforms of the phase-uncorrected extended X-ray absorption fine structure (EXAFS) spectra of the different catalysts and selected reference materials. The spectrum of LD-Cu shows both Cu−O and Cu−Cu features, confirming the presence of a mixture of Cu metal and Cu_2O. For the Cu NPs, only a Cu−Cu coordination shell associated with Cu metal can be observed, in qualitative agreement with the findings of powder X-ray diffraction analyses (Supplementary Fig. 13). Transmission electron microscopy (TEM) was employed to investigate the nanostructure of LD-Cu and the spatial dispersion of Cu_2O and Cu metal. High-angle annular dark-field scanning TEM (HAADF-STEM) imaging and energy-dispersive X-ray spectroscopy (EDX) elemental mapping showed overlapping Cu and O signals on a carbon substrate (Fig. 3d and Supplementary Figure 14), with notable variation in the intensities of the Cu and O signals from point to point on the sample. Elemental analysis further revealed an average Cu/O atom ratio of 2.7 ± 0.3 (Supplementary Table 2). Because the applied cathodic potential cannot reduce Al^{3+} to metallic Al ($Al^{3+}+3e^-\rightarrow Al$, $E°=-1.66$ V), the Al(III) in CuAl-LDH was hydrolysed and dissolved in the alkali electrolyte in the form of $[Al(OH)_4]^-$ after the initial electroreduction process[31]. Only trace amounts of Al were found in LD-Cu (0.008 mass per cent, measured by inductively coupled plasma atomic emission spectroscopy), indicating that Al acts as a sacrificial template and contributes little to acetylene electroreduction[32]. High-resolution TEM (HRTEM) images confirmed the coexistence of both Cu metal and Cu_2O nanoparticles in LD-Cu (Fig. 3e,f and Supplementary Fig. 15). Scans 1 and 2 in Supplementary Fig. 15 (and marked in Fig. 3f) show lattice fringes with a spacing of 0.180 nm, corresponding to

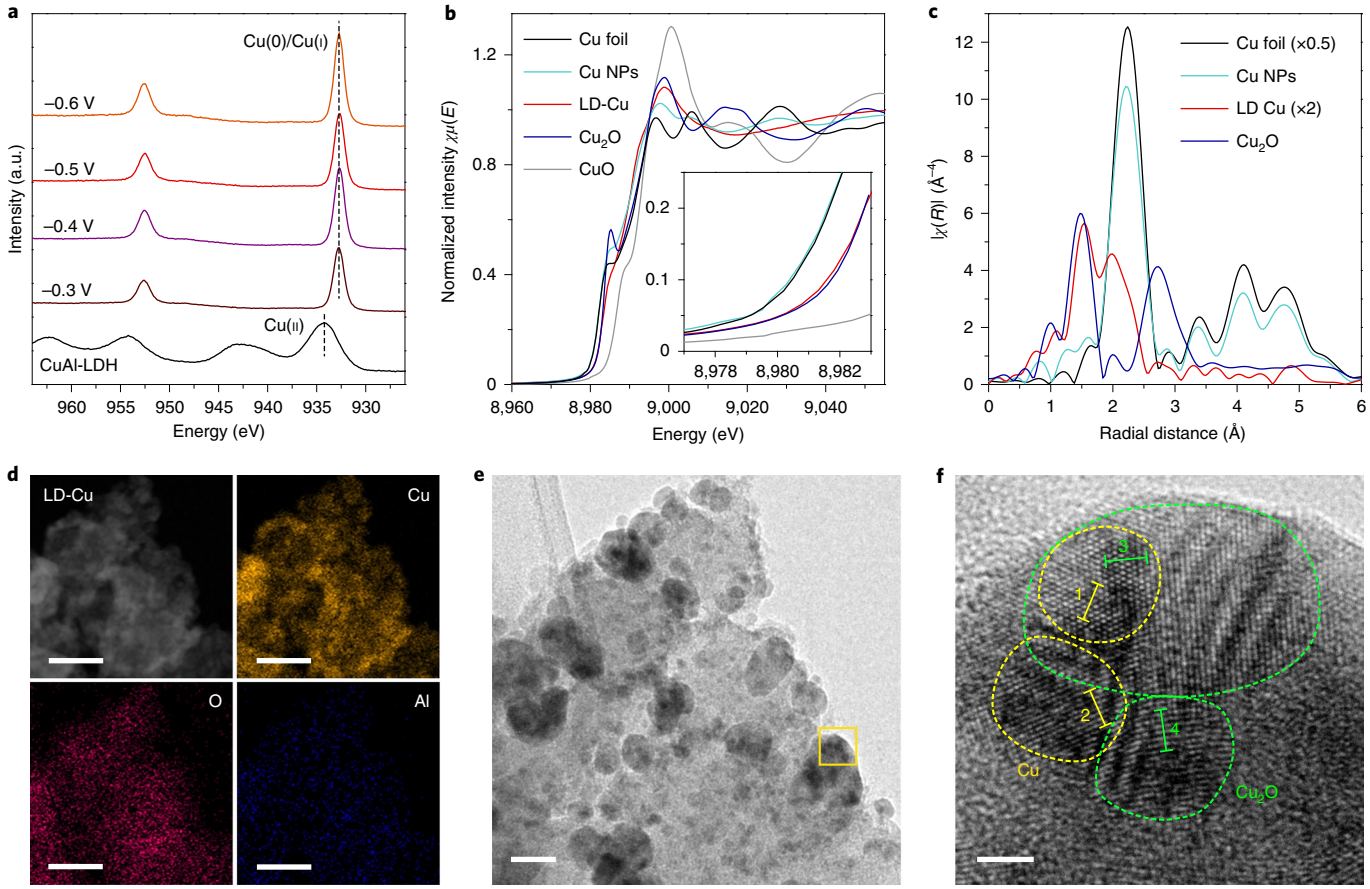

Fig. 3 | Characterization of the LD-Cu catalyst. a, Cu 2*p* XPS spectra for CuAl-LDH and LD-Cu under different potentials. **b**, Cu K-edge XANES profiles for LD-Cu, Cu NPs, Cu foil, Cu_2O and CuO (inset shows the enlarged pre-edge region from 8,977 eV to 8,983 eV). **c**, Cu K-edge EXAFS spectra in *R* space for LD-Cu, Cu NPs, Cu foil and Cu_2O. The spectra of LD-Cu and the Cu foil have been enlarged and reduced in size, respectively, to allow meaningful comparison. **d**, HAADF-STEM image of LD-Cu and the corresponding Cu, O and Al elemental maps. Scale bars, 50 nm. **e**, TEM image of LD-Cu. Scale bar, 20 nm. **f**, HRTEM image of LD-Cu, showing an enlargement of the selected region in **e**. Scale bar, 2 nm.

Cu(200) planes, whereas scans 3 and 4 show lattice fringes with a spacing of 0.213 nm, corresponding to Cu_2O(200) planes. Because the Cu metal and Cu_2O domains overlap, the active Cu species in LD-Cu is likely to be a Cu(0)/Cu(I) heterostructure with abundant Cu/Cu_2O interfaces. Further control experiments revealed that the ethylene current density decreased 2.8-fold on reducing the LD-Cu with hydrogen, and no obvious EAR enhancement was observed for physically mixed Cu and Cu_2O nanoparticles with respect to Cu NPs (Supplementary Figs. 16 and 17).

To better understand the origins of the acetylene electroreduction activity and ethylene selectivity, density functional theory calculations were then performed. Details of the computational methods and models can be found in the Supplementary Methods and Supplementary Fig. 18. The LD-Cu catalyst was modelled by a Cu/Cu_2O heterostructure, in accord with experimental observations and EXAFS fitting results (Supplementary Fig. 19 and Supplementary Table 3), and Cu(200) and Cu(111) were used to model the Cu NPs catalyst. The atomic coordinates of the optimized models are provided in Supplementary Data 1. We first investigated the projected densities of states of C_2H_2 adsorption. As shown in Fig. 4a, the Cu 3*d* orbitals overlap with the π orbitals of C_2H_2 and are about 4 eV lower in energy than the π^* orbitals, indicating that the adsorbate state is mainly ruled by d–π interactions[33]. The π orbitals are broadened and split into d–π bonding and antibonding orbitals below and above the original energy level when coupling to the Cu 3*d* orbitals in both Cu(200) and Cu/Cu_2O. Compared with Cu(200), the *d*-band centre (ε_d) of Cu/Cu_2O is narrower and shifted upwards from −2.49 to −1.98 eV, contributing to the formation of d–π antibonding orbitals above the Fermi level (ε_F)[34]. The additionally formed empty orbitals could facilitate electron transfer from hydrogen to acetylene, and suggest a further reduced activation energy for acetylene hydrogenation on Cu/Cu_2O. Figure 4b and Supplementary Fig. 20 show the energy profiles and intermediate configurations for the hydrogenation of acetylene to ethane on the different model surfaces. Acetylene spontaneously adsorbs strongly on the Cu(200) and Cu/Cu_2O surfaces. The formation of a Cu/Cu_2O interface reduces the adsorption energy of acetylene from −1.77 to −1.24 eV, but the stability of the adsorbed acetylene and transition-state (TS) energies still favour hydrogenation to ethylene rather than desorption. For the first hydrogenation step, an endothermic process with a TS energy barrier of 0.64 eV was calculated over Cu(200). In contrast, the Cu/Cu_2O structure provides an exothermic hydrogenation process, accompanied by reduced energy barriers for the first and second hydrogenation steps. The computational data thus strongly indicate that the Cu/Cu_2O structure is a suitable candidate for acetylene activation and hydrogenation to ethylene, which was verified experimentally by the 90 mV higher ethylene production onset potential for LD-Cu (−0.39 V) compared with Cu NPs (−0.48 V).

The energy barriers for ethylene desorption and activation are the dominant parameters determining product selectivity, especially in ethylene-rich conditions[35]. The reaction on Cu/Cu_2O was

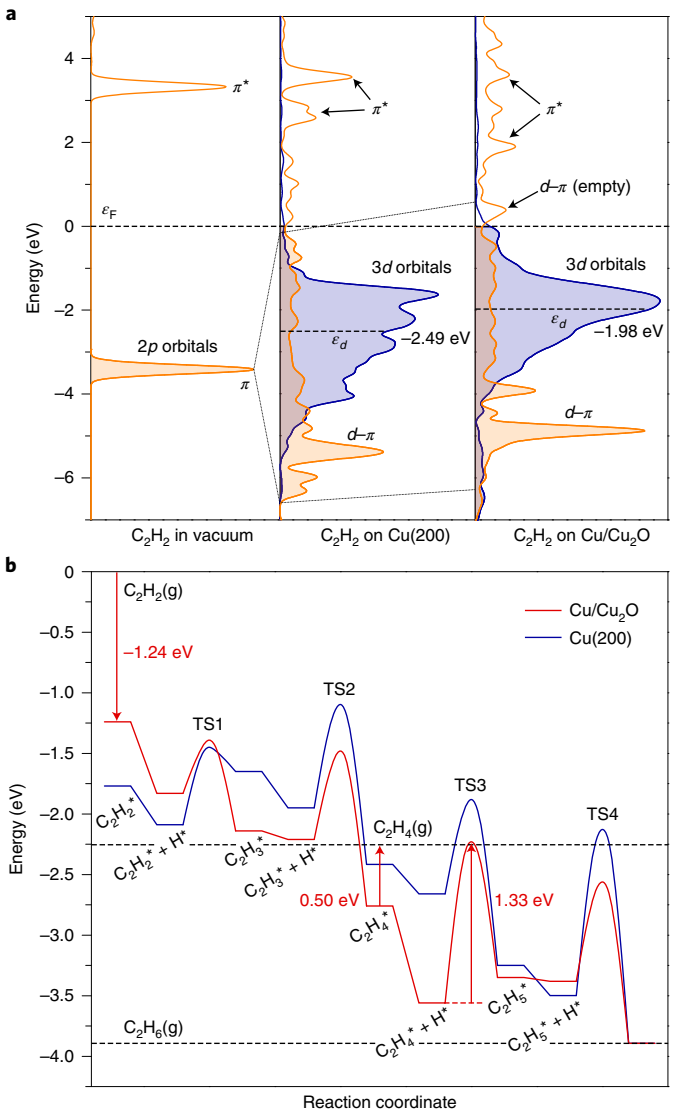

Fig. 4 | Kinetic analysis of the acetylene reduction. a, Projected electronic densities of states of the C 2*p* orbitals of C_2H_2 in a vacuum, and of the Cu 3*d* orbitals and the C 2*p* orbitals of C_2H_2 adsorbed on Cu(200) and Cu/Cu_2O. **b**, Energy profiles for the hydrogenation of acetylene on Cu/Cu_2O and Cu(200). Asterisks indicate the adsorption state of the active species.

calculated to have a barrier of 1.33 eV for the third hydrogenation step, which is significantly greater than the ethylene desorption energy (0.50 eV), suggesting that ethylene will desorb rather than undergo further reaction. Cu(200) shows a similar trend, which is in good general agreement with the low selectivity towards ethane over LD-Cu and other copper-based control samples investigated in this work (Supplementary Fig. 16). In addition, Cu/Cu_2O shows a Gibbs free energy for H* adsorption (ΔG_{H^*}) of −0.37 eV (Supplementary Table 4), which is more negative than the ΔG_{H^*} for H* adsorption on Cu(200) and Cu(111) (0.11 and 0.19 eV, respectively). Generally, materials with $|\Delta G_{H^*}|$ values larger than 0.2 eV are considered to be catalytically inert for the HER[36,37]. The value of ΔG_{H^*} for Cu/Cu_2O indicates that the desorption of H* to generate H_2 is difficult, suggesting that LD-Cu is thermodynamically unfavourable for hydrogen evolution.

Electroreduction of acetylene in an ethylene-rich gas mixture. The performance of the LD-Cu catalyst in the EAR in the presence of ethylene was subsequently investigated. All experiments were performed at room temperature (20 °C) using a simulated ethylene-rich gas source (0.5% C_2H_2, 20% C_2H_4 balanced with Ar). The gas flow rate and gas chamber structure were investigated as additional variables for this electrochemical reaction conducted under flow conditions[38,39]. The methods used to calculate the acetylene conversion and ethylene selectivity can be found in the Methods section. Due to the presence of abundant ethylene in the feed gas, the ethylene production selectivities were calculated on a carbon basis (with the exception of H_2). The acetylene conversions at different feed gas flow rates in a 0.5-cm^2 plane gas chamber, as used in the above tests, are shown in Fig. 5a. Through cathodic potential regulation, over 98% acetylene was converted at a flow rate of 1 ml min^{-1}, with the best conversion being observed at potentials between −0.4 and −0.5 V. Higher flow rates resulted in a decrease in acetylene conversion (88.9 and 33.4% conversions were achieved for flow rates of 5 and 20 ml min^{-1}, respectively). The EAR was then investigated over time at a fixed flow rate of 1 ml min^{-1}. Under these conditions, the theoretical total current needed for 100% conversion of acetylene was calculated to be 0.67 mA (see the Methods for the calculation). As can be seen from Fig. 5b, the acetylene conversion ratio remained constant at 99.1 ± 0.4%. Importantly, ethylene was the major product of acetylene electroreduction, with an average selectivity for ethylene of 93.2 ± 0.6% achieved over 5 h of operation (6.3 and 0.5% for C_4 olefins and ethane, respectively). A H_2 volume percentage of 0.07 ± 0.02 vol.% was maintained in the outlet stream, indicating that the competing HER was effectively suppressed. Unlike the acetylene conversion ratio, the product selectivities showed much less sensitivity to the gas flow rate (Fig. 5c and Supplementary Fig. 21). Even when the flow rate was increased to 20 ml min^{-1}, the ethylene selectivity remained above 90%. In addition, any H_2 generated was diluted at the higher flow rates (Supplementary Fig. 22). Importantly, the acetylene conversion was found to be highly dependent on the gas chamber area (or electrode area), as shown in Fig. 5d. For a flow rate of 10 ml min^{-1}, the acetylene conversion at a 0.5 cm^2 electrode was less than 50%, whereas over 99% acetylene conversion was achieved for an electrode area of 2.0 cm^2. Meanwhile, the H_2 volume percentage decreased when the electrode area was increased from 0.5 to 2.0 cm^2 owing to the increase in cathodic potential from −0.63 to −0.46 V (Supplementary Fig. 23). A cycling test showed that the C_2H_2 conversion and product selectivity maintained good stability with high conversion over 15 h of operation (Supplementary Fig. 24).

To further improve the acetylene conversion performance at higher flow rates and to evaluate the application prospects of the EAR, an enlarged two-electrode flow reactor containing a serpentine-type gas chamber with a geometric electrode area of 25.0 cm^2 was developed (Fig. 6a,b and Supplementary Fig. 25). NiFe-LDH nanosheets deposited on a carbon-based gas diffusion electrode was used as the anode for the oxygen evolution reaction (OER; Supplementary Fig. 26). EAR experiments in this enlarged flow reactor were performed at a flow rate of 50 ml min^{-1} (gas hourly space velocity = 4.0×10^3 l g^{-1} h^{-1}). As shown in Fig. 6c, an average acetylene conversion of 99.9 ± 0.1% was maintained over 4 h of operation, showing a high C_2H_2 conversion specific rate of 834 mmol g^{-1} h^{-1} (24.8 μmol cm^{-2} h^{-1}). The ethylene/acetylene volume ratio in the product gas exceeded 1×10^5, satisfying the purity requirement for a polyethylene-grade ethylene feedstock (Supplementary Fig. 27 and Supplementary Table 5). Further, the process maintained a very low hydrogen volume percentage of 0.08 ± 0.01% in the outlet stream. As shown in Fig. 6d, the product distribution achieved over LD-Cu in the enlarged flow reactor was similar to that of the small reactor at the slow flow rate shown in Fig. 5b, with an average ethylene selectivity of 90.1 ± 0.8% (9.2 ± 0.9 and 0.68 ± 0.12% for C_4 olefin and ethane, respectively). During this experiment, the cell voltage slightly increased from 1.95 to 1.98 V

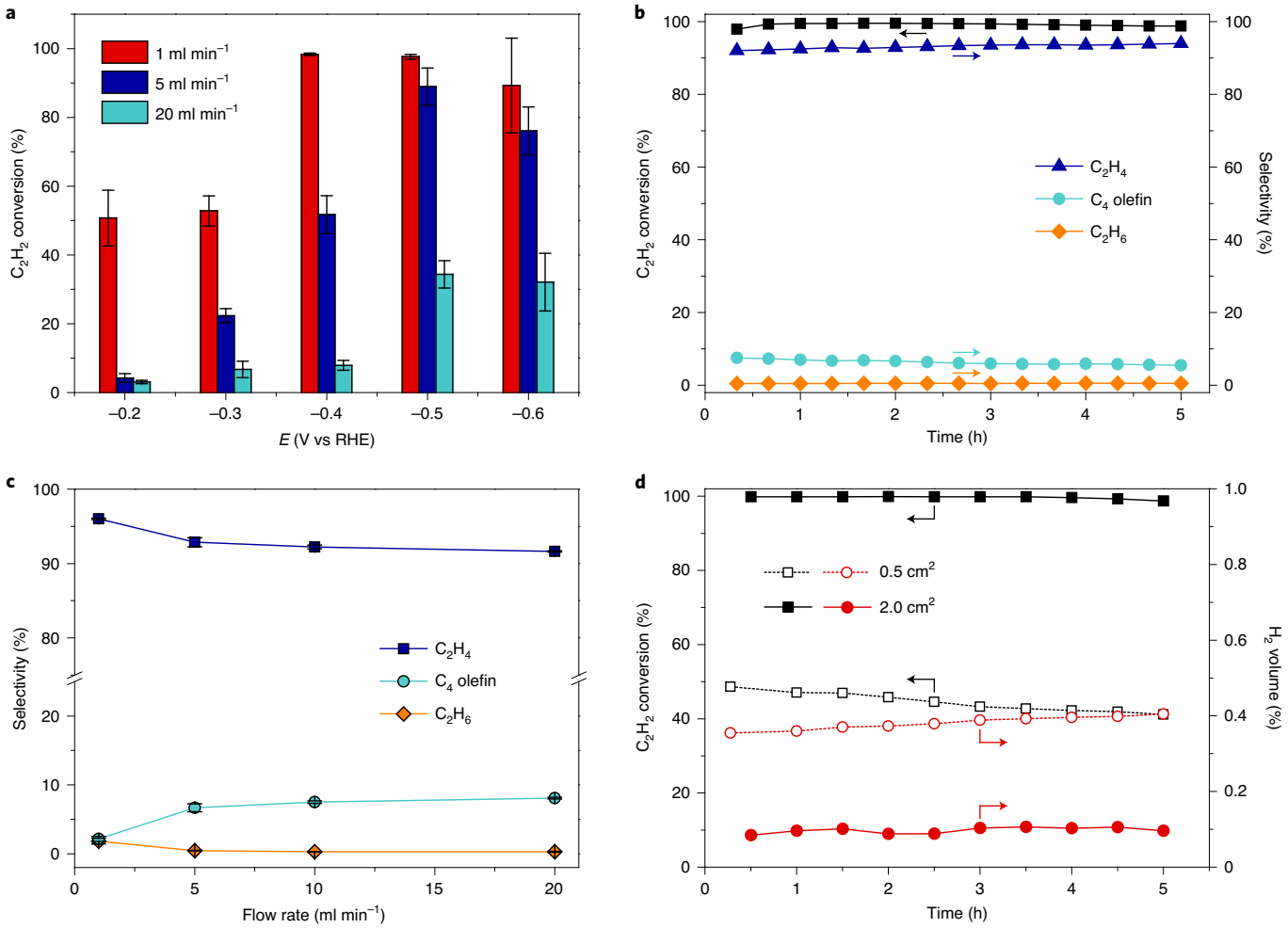

Fig. 5 | EAR in the presence of ethylene. a, Acetylene conversion over the LD-Cu catalyst for different cathodic potentials and flow rates. **b**, Time-dependent acetylene conversion and product selectivities at a flow rate of 1 ml min^{-1} and a constant current of 0.7 mA. **c**, Acetylene reduction product selectivities plotted against gas flow rate at −0.5 V vs RHE. **d**, Time-dependent acetylene conversion and H_2 volume percentage over electrodes with different areas at a flow rate of 10 ml min^{-1} and a constant current of 6.9 mA. Gas feed: 0.5% C_2H_2, 20% C_2H_4 balanced with Ar. The error bars represent the standard deviation from at least three independent measurements. Arrows in **b** and **d** indicate which axis to read off.

(Fig. 6e), which was possibly caused by the instability of the LD-Cu catalyst or the electrolyte penetration effect due to the GDL becoming less hydrophobic during the experiment (the water contact angle on the GDL side reduced from 149° before to 112° after the experiment)[40]. As shown in Fig. 6f and Supplementary Table 6, the EAR process over LD-Cu (in terms of acetylene conversion and ethylene selectivity) compares favourably with state-of-the-art thermal hydrogenation catalysts[5,6,41–43], while exhibiting the special advantages of room-temperature operation and high-purity ethylene production with negligible residual hydrogen.

Discussion

Herein we have reported the successful development of a room-temperature acetylene electroreduction system that can operate at high flow rates with near 100% acetylene conversions and ethylene selectivities of >90%. However, some critical issues still need to be addressed before this electrochemical strategy can be applied on a large scale. Although over-hydrogenation to ethane can be effectively suppressed by this electrochemical route, controlling acetylene dimerization at low overpotentials needs to be addressed to further increase the ethylene selectivity. In addition, the full cell acetylene reduction experiments performed here were operated ~1.5 V above the thermodynamic potential. This results in a cell energy efficiency of only ~21% (see Methods for details), which will increase the electricity cost required for the process. In this work, the OER was used as the proton source for the acetylene reduction, although potentially this could be replaced by another value-added anode reaction that is less energetic. For example, the selective oxidation of low cost and readily available alcohols (for example, glycerol and benzyl alcohol) has recently been demonstrated to be a possible alternative to the OER as a source of protons[44,45]. Hence, it should be possible to improve the cell energy efficiency through both cathode and anode engineering. At today's electricity prices, the EAR system developed in this work would use around US$4.4 in electricity to remove acetylene residues from 1 tonne of raw ethylene stock, which represents less than 0.5% of the ethylene market price (see Supplementary Methods for details), suggesting its potential for large-scale ethylene gas purification.

Considering the massive scale of the polyethylene industry, the atom and energy economies of acetylene-to-ethylene conversion are important evaluation criteria that need to be considered. As shown in Fig. 6g, for acetylene conversion to ethylene through the conventional hydrogenation route, H_2 production consumes most of the total energy needed for the process because the acetylene

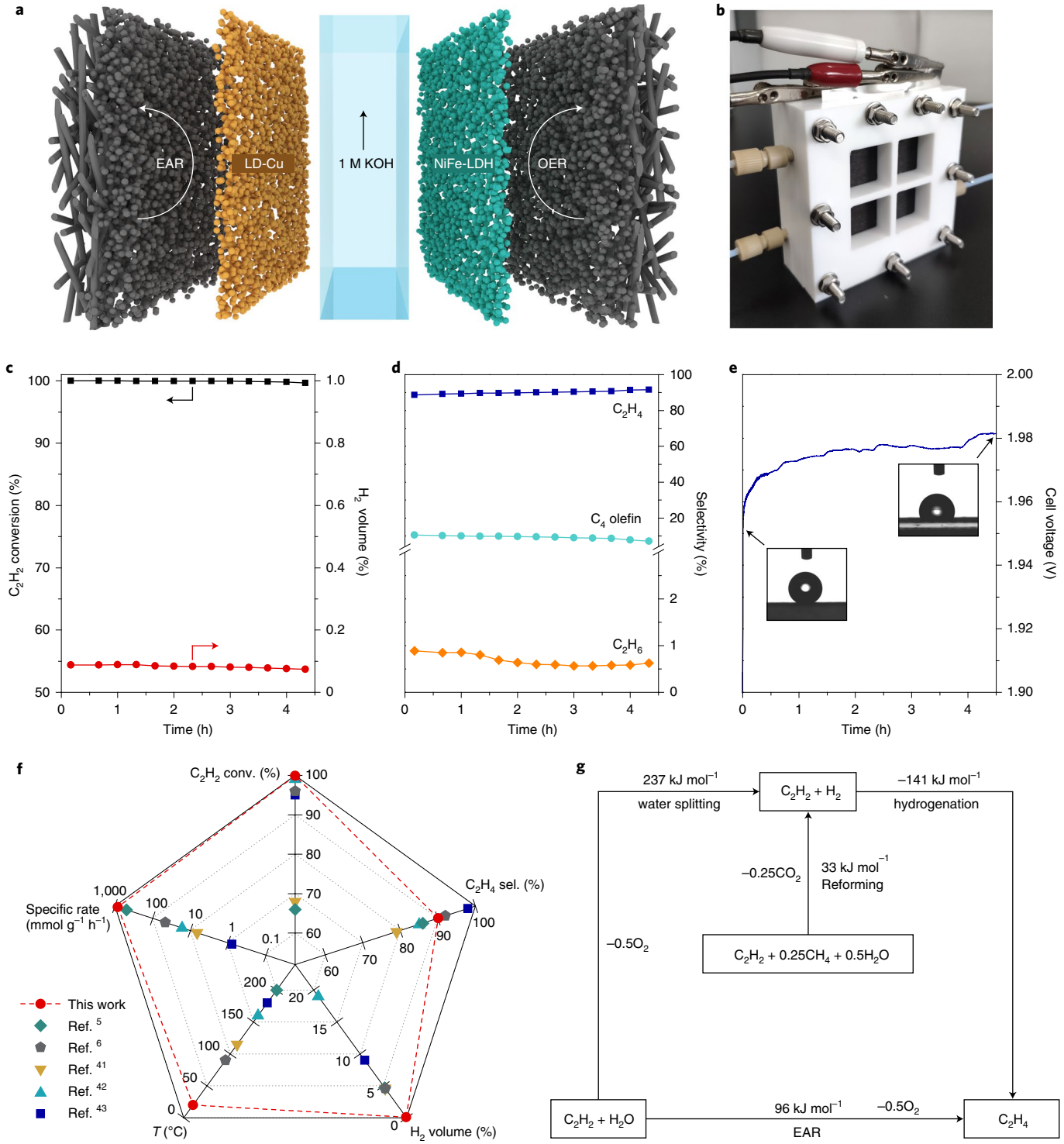

Fig. 6 | Full cell EAR performance evaluation and comparison. a, Schematic illustration of the two-electrode EAR flow cell. **b**, A photograph of the assembled flow reactor. **c**–**e**, Full cell EAR experiments showing acetylene conversion and H_2 volume percentage (**c**), product selectivity (**d**) and cell voltage (**e**) at a constant current of 35 mA in 1 M KOH. Gas feed: 0.5% C_2H_2, 20% C_2H_4 balanced with Ar at a gas flow rate of 50 ml min^{-1}. The arrows in **c** indicate which axis to read off. The insets in **e** show photographs of water droplets on the cathodic GDL before and after the EAR experiment. **f**, Comparison of the performance of the LD-Cu-based EAR system with previous state-of-the-art acetylene hydrogenation catalysts[5,6,41–43]. conv., conversion; sel., selectivity. **g**, Atom and energy economies of different acetylene-to-ethylene conversion routes. Standard Gibbs free energies (expressed as kJ per mole acetylene) are indicated for each pathway.

hydrogenation reaction is spontaneous (standard Gibbs free energy, $\Delta G = -141$ kJ mol^{-1}). Steam reforming of methane and water splitting are two typical H_2 production technologies. Steam reforming of methane has a relatively low ΔG of 33 kJ mol^{-1}, but yields 0.25 equivalents of CO_2 for each molecule of C_2H_2 hydrogenated[46]. Water splitting for H_2 production is CO_2-free but is thermodynamically

unfavourable ($\Delta G = 237\,kJ\,mol^{-1}$), meaning that the tandem water splitting–acetylene hydrogenation route is energetically wasteful[47]. In contrast, the EAR process represents a one-step strategy that has both a low theoretical energy input requirement ($\Delta G = 96\,kJ\,mol^{-1}$) and is atom efficient (that is, it does not contribute to greenhouse gas emissions, as long as the electricity used to drive the reaction is sourced from renewables). Considering the atom and energy economies alongside performance, the room-temperature electrochemical reduction of acetylene in ethylene-rich streams appears to be a green and effective approach compared with conventional thermal hydrogenation routes and should attract the attention of the plastics industry.

Methods

Synthesis of the catalysts. To prepare the CuAl-LDH nanosheets, 1.06 g Na_2CO_3 (AR, ≥99.5%, Shanghai Macklin Biochemical) was dissolved in 180 ml deionized water (to give solution A). Next, 3.62 g $Cu(NO_3)_2{\cdot}3H_2O$ (AR, ≥99.5%, Tianjin Yongda Chemical Reagents) and 1.88 g $Al(NO_3)_3{\cdot}9H_2O$ (AR, 99.0%, Shanghai Aladdin Biochemical Technology) were dissolved in 20 ml deionized water (to give solution B). Finally, 1.8 g NaOH (AR, ≥96%, Xilong Scientific) was dissolved in 30 ml deionized water (to give solution C). Solutions B and C were then simultaneously added dropwise to solution A under constant stirring. Throughout the synthesis, the pH of the solution was kept constant (9.5) and monitored with a pH meter (FE20, Mettler Toledo). After the addition of solutions B and C, a sky-blue suspension was obtained. The solid product was collected by centrifugation (8,000 r.p.m.) and then washed five times with deionized water. The as-prepared CuAl-LDH nanosheets were then redispersed in deionized water and kept at 2 °C in a refrigerator for later use. The CuAl-LDH concentration was typically 6.0 mg ml^{-1}. The Cu/Al atom ratio in the as-prepared CuAl-LDH nanosheets was determined to be 2.5.

To prepare Cu_2O nanoparticles (Cu_2O NPs), 500 µl of a 0.1 M $CuSO_4$ (AR, Tianjin Pharmaceutical Group) solution was added to a beaker containing 50 ml deionized water. Subsequently, 1.75 ml of a 1.0 M NaOH solution was added to the beaker under vigorous stirring to form a blue precipitate. Upon addition of 2.5 ml of 0.2 M ascorbic acid under constant stirring (AR, Macklin Reagent), the solution gradually turned bright yellow. After stirring for 10 min, the nanoparticle product was collected by centrifugation at 8,500 r.p.m. for 10 min and then washed several times with a water–ethanol mixture (1:1). The precipitate was then dried at 60 °C for 4 h for storage.

Preparation of the working electrode. To prepare the LDH-derived copper catalyst (LD-Cu) electrodes, the as-prepared CuAl-LDH nanosheet aqueous dispersion was first diluted with ethylene glycol and *n*-propyl alcohol to form a water–ethylene glycol–*n*-propyl alcohol mixed-solvent ink (volume ratio 1:1:1) in which the CuAl-LDH concentration was 0.5 mg ml^{-1}. For experiments using an electrochemical cell of geometric area 0.5 cm^2, 70 µl of the ink was drop-coated onto a carbon-based GDL (H14C9, Freudenberg Group) and dried under an infrared lamp. For experiments with an electrochemical cell of geometric area 2.0 cm^2, 280 µl of the ink was drop-coated onto a carbon-based GDL (H14C9, Freudenberg Group) and dried under an infrared lamp. The as-prepared gas diffusion electrodes were then connected to an electrochemical cell for the in situ electroreduction of the supported CuAl-LDH (see the Electrochemical measurements section for more details). The CuAl-LDH electroreduction was typically conducted at −0.4 V for 10 min in 1 M KOH immediately before further electrochemical measurements.

To prepare hydrogen-reduced LD-Cu (LD-Cu-H_2), the electroreduced LD-Cu electrode was removed from the electrochemical cell, rinsed with water and dried. Then, the electrode was transferred to a crucible inside a tube furnace and heated in a 10% H_2–Ar gas mixture at 300 °C for 5 h (heating rate 5 °C min^{-1}, flow rate 200 ml min^{-1}). The obtained LD-Cu-H_2 electrode was then removed from the furnace after naturally cooling to room temperature.

To prepare the metallic Cu NP electrodes, commercial Cu nanoparticles (99.9% metals basis, 10–30 nm, Shanghai Macklin Biochemical) were first dispersed in water–ethylene glycol–*n*-propyl alcohol (volume ratio 1:1:1) to form an ink with a Cu NP concentration of 0.5 mg ml^{-1}. The ink was then applied to the carbon-based GDL (H14C9, Freudenberg Group) with all other procedures, including the in situ electroreduction treatment, the same as those described above for LD-Cu.

To prepare the Cu_2O NP electrodes, the as-prepared Cu_2O NPs were dispersed in water–ethylene glycol–*n*-propyl alcohol (volume ratio 1:1:1) to form an ink with a Cu_2O NP concentration of 0.5 mg ml^{-1}. Then, 70 µl of the ink was drop-coated onto a carbon-based GDL and dried under an infrared lamp to achieve a loading area of 0.5 cm^2.

To prepare physically mixed Cu and Cu_2O NP electrodes (Cu+Cu_2O), commercial Cu NPs and the as-prepared Cu_2O NPs (mass ratio 1:1) were dispersed in water–ethylene glycol–*n*-propyl alcohol (volume ratio 1:1:1) and then stirred to form a uniform ink with a nanoparticle concentration of 0.5 mg ml^{-1}. Then, 70 µl of the ink was drop-coated onto a carbon-based GDL and dried under an infrared lamp to achieve a loading area of 0.5 cm^2.

Synthesis of the NiFe-LDH nanosheets. NiFe-LDH nanosheets were prepared by a previously reported method[48]. Briefly, 20 ml of an aqueous solution containing 2.181 g $Ni(NO_3)_2{\cdot}6H_2O$ (Beijing Chemical Works) and 1.010 g $Fe(NO_3)_3{\cdot}9H_2O$ (Beijing Chemical Works) was added dropwise to an aqueous 23 vol.% formamide solution (20 ml, Beijing Chemical Works) under magnetic stirring at 80 °C. Simultaneously, 2.5 M NaOH solution was added dropwise to maintain a pH of ~10. The reaction was completed within 10 min. After cooling to room temperature, the product was collected by centrifugation at 12,000 r.p.m., washed alternately with deionized water and ethanol five times in total, and then redispersed in water for subsequent use.

Electrochemical measurements. The electrochemical experiments were performed using a CHI660E electrochemical workstation (Shanghai Chenhua). A platinum electrode and Ag/AgCl (saturated KCl) electrode were used as the counter and reference electrodes, respectively. A 1 M KOH solution was used as the electrolyte (unless otherwise stated). Two types of flow cells were used for the electrochemical measurements, with the cells differing in the design of the gas flow chamber. The three-electrode flow cell had a gas chamber with an electrode area of 0.5 cm^2, as shown in Supplementary Fig. 3. The two-electrode flow cell had a 25.0-cm^2 serpentine-type gas chamber, as shown in Supplementary Fig. 25. Electrode potentials were rescaled to the RHE using the following equation:

$$E_{RHE} = E_{Ag/AgCl} + 0.1976 + 0.0591 \times pH \quad (1)$$

Before the measurements, the working electrode (LD-Cu or Cu NPs) was first positioned at the interface between the gas flow chamber and the cathodic chamber. The gas chamber was then purged with the reactant gas (5.0 vol.% C_2H_2 in Ar) at a flow rate of 30 ml min^{-1} for 5 min, with the gas flow rate being controlled by a mass flowmeter (Sevenstar, D07-19B). Then, both the cathodic and anodic chambers of the electrochemical cell were filled with 5 ml of 1 M KOH. Subsequently, the three electrodes were connected to the electrochemical workstation. The resistance of the system was tested before each in situ electroreduction treatment or EAR measurement to minimize interferences (<5 Ω). No *iR* correction was applied during the measurements.

For EAR experiments in the absence of ethylene, a reactant mixture of 5.0 vol.% C_2H_2 with Ar balance was introduced. For EAR experiments in the presence of excess ethylene, a reactant mixture of 0.5 vol.% C_2H_2, 20.0 vol.% C_2H_4 and 79.5 vol.% Ar was used. All electrochemical measurements except stability tests were carried out for 30 min, with gas samples being taken from the outlet stream by a syringe for analysis. The gas samples were analysed using a gas chromatograph (GC-2014C, Shimadzu) equipped with three channels. The first channel analysed hydrocarbons using a HP PLOT Al_2O_3 column for separation, He as the carrier gas and a flame ionization detector. The second channel analysed CO_2, N_2, Ar, O_2, CH_4 and CO using a micropacket Haysep Q H-N column and a MolSieve 13X column for separation, He as carrier gas and a thermal conductivity detector (TCD). The third channel analysed H_2 using a micropacket HayeSep Q and MolSieve 5 Å column, N_2 as the carrier gas and a TCD detector. The products of the isotope experiment performed with D_2O (99.9%, Innochem Technology) were identified using gas chromatography mass spectrometry (GCMS, 7890A, Agilent Technologies) with a 60 m GS-Carbonplot column feed to the mass spectrometer.

Performance calculations. The partial current densities (j) of the cathodic products were calculated as follows:

$$j = \frac{av}{\beta s} \times \frac{zFP}{RT} \quad (2)$$

where a is the peak area of the products detected by gas chromatography, β is the conversion factor for the detected product based on the external standard method of gas chromatography, v is the velocity of gas flow, s is the electrode area, z is the electron transfer number, F is the Faraday constant (96,485 C mol^{-1}), P is the atmospheric pressure (101.325 kPa), R is the molar gas constant (8.314 J mol^{-1} K^{-1}) and T is the reaction temperature. The Faradaic efficiency (FE) of the cathodic products was calculated using the following formula:

$$FE(\%) = \frac{j}{J} \times 100 \quad (3)$$

where J is the total current density. The acetylene conversion (C) and selectivity (S) for ethylene were calculated as follows:

$$C(\%) = \frac{c_{feed} - c_x}{c_{feed}} \times 100 \quad (4)$$

$$S(\%) = \frac{c_{feed} - c_x}{c_{feed} - c_x + [C_2H_6] + 2[C_4H_x]} \times 100 \quad (5)$$

where c_{feed} represents the acetylene concentration in the feed and c_x, $[C_2H_6]$ and $[C_4H_x]$ are the concentrations of acetylene, ethane and C_4 olefins in the product. To calculate the selectivity, it was assumed that acetylene was hydrogenated only to ethylene, which in turn may be hydrogenated to ethane[49]. Only C_2 and C_4 hydrocarbons were detected in our electrochemical experiments, and the carbon balance (total carbon atoms in the detected products/total carbon atoms in the feed gas) was between 98% and 99%.

The H_2 volume in the outlet stream was calculated as follows:

$$H_2\ \text{volume}\ (\%) = \frac{V_{H,g}}{V_{feed}} \times 100 \quad (6)$$

$$H_2\ \text{volume}\ (\%) = \frac{V_{H,f} - V_C \times C}{V_{feed}} \times 100 \quad (7)$$

where $V_{H,g}$ is the volume of generated H_2, V_{feed} is the volume of the gas feed, $V_{H,f}$ is the volume of H_2 in the gas feed, V_C is the volume of acetylene in the gas feed and C is the acetylene conversion ratio. Equation (6) was used for the EAR experiments in this study, whereas equation (7) was used for the hydrogenation experiments in previous reference works. In equation (6), the volume of feed gas is assumed to be constant. In equation (7), it is assumed that H_2 is only consumed by C_2H_2 hydrogenation.

The theoretical current (I_T) needed for 100% conversion of acetylene was calculated as follows:

$$I_T = \frac{zFPv'}{RT} \quad (8)$$

where z is the electron transfer number (equals 2 for the reduction of acetylene to ethylene), F is the Faraday constant, P is the atmospheric pressure, v' is the velocity of acetylene, R is the molar gas constant and T is the temperature (293.15 K). For an ethylene-rich gas source (0.5% C_2H_2, 20% C_2H_4 balanced with Ar) with a flow rate of 1 ml min^{-1}, $v' = 8.3 \times 10^{-8}$ l s^{-1} and the theoretical total current was calculated to be 0.67 mA.

The cell energy efficiency (EE) for ethylene production from the simulated gas mixture by EAR was calculated using the following equation:

$$EE\ (\%) = \frac{\Delta G_r R\,(C_2H_2)\,S\,(C_2H_4)}{UI} \times 100 \quad (9)$$

where ΔG_r is the reaction Gibbs energy of the acetylene reduction reaction ($C_2H_2 + H_2O \rightarrow C_2H_4 + 1/2\,O_2$), which is 96 kJ mol^{-1}, $R(C_2H_2)$ is the conversion rate of acetylene, $S(C_2H_4)$ is the selectivity of ethylene, U is the cell voltage and I is the total current of the reaction. From the full cell experiment, $R(C_2H_2)$ and $S(C_2H_4)$ were measured to be 1.7×10^{-7} mol s^{-1} and 90.1%, respectively, and U and I were determined to be ~1.98 V and 0.035 A, respectively. The cell energy efficiency of the full cell was calculated to be ~21%.

Data availability

The data that support the plots within this paper and other findings of this study are available from the corresponding authors on reasonable request.

Received: 1 November 2020; Accepted: 20 May 2021;
Published online: 1 July 2021

References

1. Borodziński, A. & Bond, G. C. Selective Hydrogenation of ethyne in ethane-rich streams on palladium catalysts. Part 1. Effect of changes to the catalyst during reaction. *Catal. Rev.* **48**, 91–144 (2006).
2. Lewis, J. D. Separation of acetylene from ethylene-bearing gases. US patent 3,837,144 (1974).
3. Hu, T. L. et al. Microporous metal–organic framework with dual functionalities for highly efficient removal of acetylene from ethylene/acetylene mixtures. *Nat. Commun.* **6**, 7328 (2015).
4. Kenzi, T. On the retardation of catalysis. The catalytic reaction between acetylene and hydrogen. *Bull. Chem. Soc. Jpn* **23**, 180–184 (1950).
5. Armbruster, M. et al. $Al_{13}Fe_4$ as a low-cost alternative for palladium in heterogeneous hydrogenation. *Nat. Mater.* **11**, 690–693 (2012).
6. Feng, Q. et al. Isolated single-atom Pd sites in intermetallic nanostructures: high catalytic selectivity for semihydrogenation of alkynes. *J. Am. Chem. Soc.* **139**, 7294–7301 (2017).
7. Zhou, S. et al. Pd single-atom catalysts on nitrogen-doped graphene for the highly selective photothermal hydrogenation of acetylene to ethylene. *Adv. Mater.* **31**, 1900509 (2019).
8. Feng, Q. et al. Mesoporous nitrogen-doped carbon-nanosphere-supported isolated single-atom Pd catalyst for highly efficient semihydrogenation of acetylene. *Adv. Mater.* **31**, 1901024 (2019).
9. Sárkány, A., Horváth, A. & Beck, A. Hydrogenation of acetylene over low loaded Pd and Pd-Au/SiO_2 catalysts. *Appl. Catal. A* **229**, 117–125 (2002).
10. McGown, W. T., Kemball, C. & Whan, D. A. Hydrogenation of acetylene in excess ethylene on an alumina-supported palladium catalyst at atmospheric pressure in a spinning basket reactor. *J. Catal.* **51**, 173–184 (1978).
11. Yang, H. B. et al. Atomically dispersed Ni(I) as the active site for electrochemical CO_2 reduction. *Nat. Energy* **3**, 140–147 (2018).
12. Jouny, M., Luc, W. & Jiao, F. High-rate electroreduction of carbon monoxide to multi-carbon products. *Nat. Catal.* **1**, 748–755 (2018).
13. Leow, W. R. et al. Chloride-mediated selective electrosynthesis of ethylene and propylene oxides at high current density. *Science* **368**, 1228–1233 (2020).
14. Davitt, H. J. & Albright, L. F. Electrochemical hydrogenation of ethylene, acetylene, and ethylene-acetylene mixtures. *J. Electrochem. Soc.* **118**, 236–242 (1971).
15. Rubinson, J. F., Behymer, T. D. & Mark, H. B. Direct reduction of acetylene at molybdenum modified polymeric sulfur nitride, (SN)x, electrodes. *J. Am. Chem. Soc.* **104**, 1224–1229 (1982).
16. Gao, Y., Tsuji, H., Hattori, H. & Kita, H. New on-line mass spectrometer system designed for platinum-single crystal electrode and electroreduction of acetylene. *J. Electroanal. Chem.* **372**, 195–200 (1994).
17. Bełtowska-Brzezinska, M., Łuczak, T., Mączka, M., Baltruschat, H. & Müller, U. Ethyne oxidation and hydrogenation on porous Pt electrode in acidic solution. *J. Electroanal. Chem.* **519**, 101–110 (2002).
18. Otsuka, K. & Yagi, T. An electrochemical membrane reactor for selective hydrogenation of acetylene in abundant ethylene. *J. Catal.* **145**, 289–294 (1994).
19. Huang, B., Durante, C., Isse, A. A. & Gennaro, A. Highly selective electrochemical hydrogenation of acetylene to ethylene at Ag and Cu cathodes. *Electrochem. Commun.* **34**, 90–93 (2013).
20. Mark, H. B., Rubinson, J. F., Krotine, J., Vaughn, W. & Goldschmidt, M. Catalysis of the reduction of acetylene at poly-3-methylthiophene electrodes. *Electrochim. Acta* **45**, 4309–4313 (2000).
21. García de Arquer, F. P. et al. CO_2 electrolysis to multicarbon products at activities greater than 1 A cm^{-2}. *Science* **367**, 661–666 (2020).
22. Weekes, D. M., Salvatore, D. A., Reyes, A., Huang, A. & Berlinguette, C. P. Electrolytic CO_2 reduction in a flow cell. *Acc. Chem. Res.* **51**, 910–918 (2018).
23. Chen, C., Khosrowabadi Kotyk, J. F. & Sheehan, S. W. Progress toward commercial application of electrochemical carbon dioxide reduction. *Chem* **4**, 2571–2586 (2018).
24. Li, Z. et al. Co-based catalysts derived from layered-double-hydroxide nanosheets for the photothermal production of light olefins. *Adv. Mater.* **30**, 1800527 (2018).
25. Zhao, Y. et al. Reductive transformation of layered-double-hydroxide nanosheets to Fe-based heterostructures for efficient visible-light photocatalytic hydrogenation of CO. *Adv. Mater.* **30**, 1803127 (2018).
26. Yao, D. et al. Balancing effect between adsorption and diffusion on catalytic performance inside hollow nanostructured catalyst. *ACS Catal.* **9**, 2969–2976 (2019).
27. Zhang, R. et al. Insight into the effects of Cu component and the promoter on the selectivity and activity for efficient removal of acetylene from ethylene on Cu-based catalyst. *J. Phys. Chem. C.* **121**, 27936–27949 (2017).
28. Zhang, R., Zhang, J., Jiang, Z., Wang, B. & Fan, M. The cost-effective Cu-based catalysts for the efficient removal of acetylene from ethylene: the effects of Cu valence state, surface structure and surface alloying on the selectivity and activity. *Chem. Eng. J.* **351**, 732–746 (2018).
29. Liu, Y. et al. Layered double hydroxide-derived Ni-Cu nanoalloy catalysts for semi-hydrogenation of alkynes: improvement of selectivity and anti-coking ability via alloying of Ni and Cu. *J. Catal.* **359**, 251–260 (2018).
30. Platzman, I., Brener, R., Haick, H. & Tannenbaum, R. Oxidation of polycrystalline copper thin films at ambient conditions. *J. Phys. Chem. C* **112**, 1101–1108 (2008).
31. Xiao, F., Zhang, B. & Lee, C. Effects of low temperature on aluminum(III) hydrolysis: theoretical and experimental studies. *J. Environ. Sci.* **20**, 907–914 (2008).
32. Tian, G.-L. et al. Monodisperse embedded nanoparticles derived from an atomic metal-dispersed precursor of layered double hydroxide for architectured carbon nanotube formation. *J. Mater. Chem. A* **2**, 1686–1696 (2014).
33. Zhou, Y. et al. Adsorption of acetylene on ordered Ni_xAg_{1-x}/Ni (111) and effect of Ag-dopant: a DFT study. *Appl. Surf. Sci.* **435**, 521–528 (2018).
34. Bligaard, T. & Nørskov, J. K. Ligand effects in heterogeneous catalysis and electrochemistry. *Electrochim. Acta* **52**, 5512–5516 (2007).
35. Studt, F. et al. Identification of non-precious metal alloy catalysts for selective hydrogenation of acetylene. *Science* **320**, 1320–1322 (2008).
36. Gao, G., O'Mullane, A. P. & Du, A. 2D MXenes: a new family of promising catalysts for the hydrogen evolution reaction. *ACS Catal.* **7**, 494–500 (2016).
37. Zhang, B., Zhou, J., Guo, Z., Peng, Q. & Sun, Z. Two-dimensional chromium boride MBenes with high HER catalytic activity. *Appl. Surf. Sci.* **500**, 144248 (2020).
38. Zheng, T. et al. Large-scale and highly selective CO_2 electrocatalytic reduction on nickel single-atom catalyst. *Joule* **3**, 265–278 (2019).

39. Li, J. et al. Efficient electrocatalytic CO_2 reduction on a three-phase interface. *Nat. Catal.* **1**, 592–600 (2018).
40. Leonard, M. E., Clarke, L. E., Forner-Cuenca, A., Brown, S. M. & Brushett, F. R. Investigating electrode flooding in a flowing electrolyte, gas-fed carbon dioxide electrolyzer. *ChemSusChem* **13**, 400–411 (2020).
41. Hu, M. et al. MOF-confined sub-2 nm atomically ordered intermetallic PdZn nanoparticles as high-performance catalysts for selective hydrogenation of acetylene. *Adv. Mater.* **30**, 1801878 (2018).
42. Pei, G. X. et al. Performance of Cu-alloyed Pd single-atom catalyst for semihydrogenation of acetylene under simulated front-end conditions. *ACS Catal.* **7**, 1491–1500 (2017).
43. Huang, F. et al. Anchoring Cu_1 species over nanodiamond-graphene for semi-hydrogenation of acetylene. *Nat. Commun.* **10**, 4431 (2019).
44. Coutanceau, C., Baranton, S. & Kouame, R. S. B. Selective electrooxidation of glycerol into value-added chemicals: a short overview. *Front. Chem.* **7**, 100 (2019).
45. Wang, D. et al. Direct electrochemical oxidation of alcohols with hydrogen evolution in continuous-flow reactor. *Nat. Commun.* **10**, 2796 (2019).
46. Wagman, D. D. The NBS tables of chemical thermodynamic properties. *J. Phys. Chem. Ref. Data* **11** (Suppl. 2) 38, 83 (1982).
47. Kudo, A. & Miseki, Y. Heterogeneous photocatalyst materials for water splitting. *Chem. Soc. Rev.* **38**, 253–278 (2009).
48. Zhang, X. et al. A simple synthetic strategy toward defect-rich porous monolayer NiFe-layered double hydroxide nanosheets for efficient electrocatalytic water oxidation. *Adv. Energy Mater.* **9**, 1900881 (2019).
49. Osswald, J. et al. Palladium–gallium intermetallic compounds for the selective hydrogenation of acetylene: part II: surface characterization and catalytic performance. *J. Catal.* **258**, 219–227 (2008).

Acknowledgements

We acknowledge financial support from the National Key Projects for Fundamental Research and Development of China (2017YFA0206904, 2017YFA0206900, 2016YFB0600901 and 2018YFB1502002), the National Natural Science Foundation of China (51825205, U1662118, 51772305, 51572270, 21871279, 21802154 and 21902168), the Beijing Natural Science Foundation (2191002, 2194089 and 2182078), the Strategic Priority Research Program of the Chinese Academy of Sciences (XDB17000000), the Beijing Municipal Science and Technology Project (Z181100005118007), a Royal Society Newton Advanced Fellowship (NA170422), the International Partnership Program of the Chinese Academy of Sciences (GJHZ1819 and GJHZ201974), the K. C. Wong Education Foundation and the Youth Innovation Promotion Association of the CAS. G.I.N.W. acknowledges funding support from the University of Auckland Faculty Research Development Fund, the Energy Education Trust of New Zealand, the MacDiarmid Institute for Advanced Materials and Nanotechnology and a philanthropic donation from G. and K. Trounson. The EXAFS experiments were conducted at the 1W1B beamline of Beijing Synchrotron Radiation Facility (BSRF).

Author contributions

R.S. and T.Z. conceived the idea for the project. R.S. designed electrochemical cell. Z.W. and Z.L. performed the structural characterization. R.S. and Z.W. conducted the measurements. Y.Z., B.Z. and Z.S. performed the computer simulation. R.S., G.I.N.W. and T.Z. wrote the manuscript and C.X. and H.W. provided suggestions. T.Z. supervised the project. All authors discussed the results and commented on the manuscript.

Competing interests

The authors declare no competing interests.

Additional information

Supplementary information The online version contains supplementary material available at https://doi.org/10.1038/s41929-021-00640-y.

Correspondence and requests for materials should be addressed to H.W. or T.Z.

Peer review information *Nature Catalysis* thanks the anonymous reviewers for their contribution to the peer review of this work.

Reprints and permissions information is available at www.nature.com/reprints.

Publisher's note Springer Nature remains neutral with regard to jurisdictional claims in published maps and institutional affiliations.